Halogen-Driven Magnetic Properties of Two-Dimensional Binary and Janus Cr_2XYSe_2 (X, Y = F, Cl, Br, I) Monolayers

S. Davoudi Tanha and Y. Mogulkoc*
Department of Physics Engineering, Faculty of Engineering, Ankara University, 06100, Ankara, Turkey

A. Mogulkoc
Department of Physics, Faculty of Science, Ankara University, 06100, Ankara, Turkey

(Dated: March 5, 2026)

I. PHONON DISPERSION SPECTRUM OF Cr_2XYSe_2

Dynamical stability was examined using phonon spectra generated with the PHONOPY code based on density-functional perturbation theory, as shown in Fig. S4.

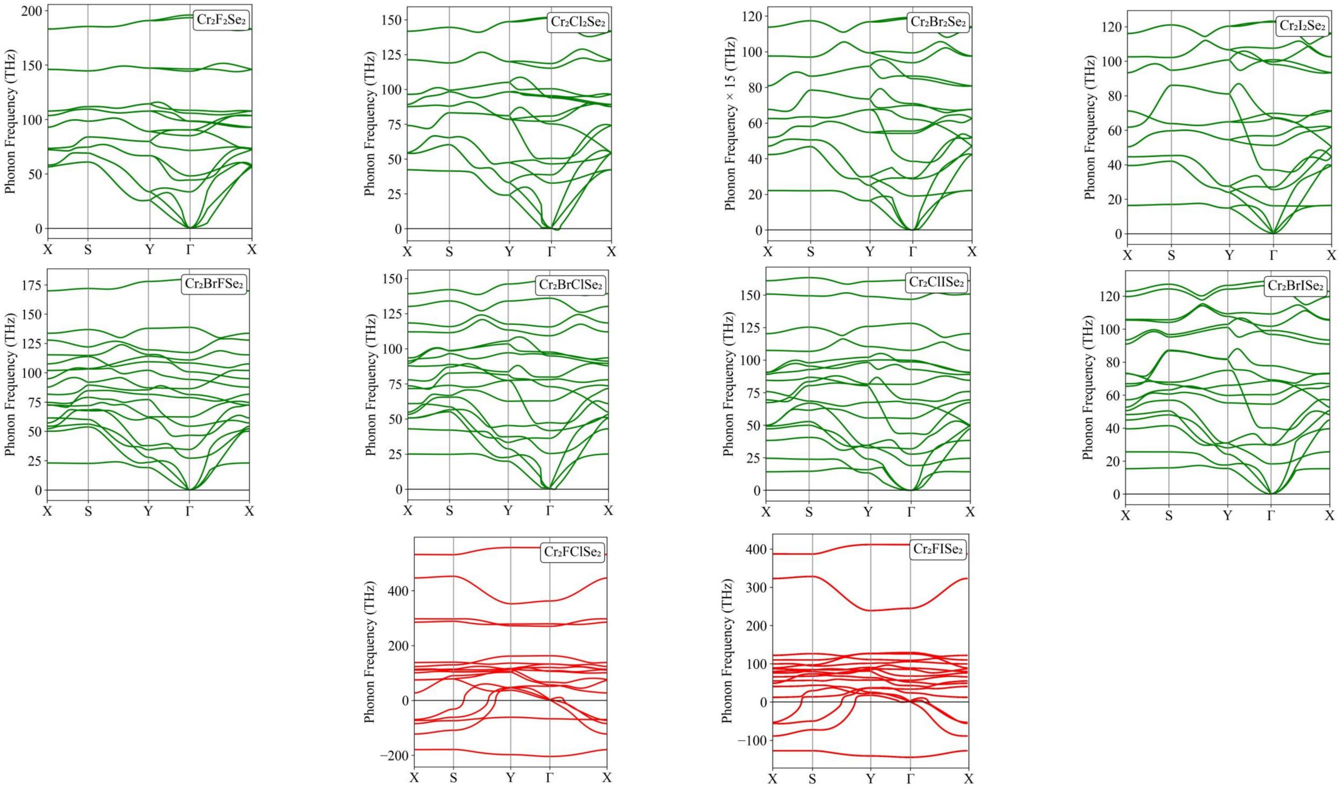

FIG. S1. Phonon spectra of the stable Cr_2XYSe_2 monolayers calculated at $U = 0$. The absence of imaginary frequencies (green curves) confirms the dynamical stability of the corresponding compositions along the high-symmetry path of the Brillouin zone. The first and second panels correspond to the binary and Janus structures, respectively. Conversely, the last panel shows imaginary phonon branches (red curves) for Cr_2FClSe_2 and Cr_2FISe_2, indicating that these compositions are dynamically unstable in the orthorhombic phase.

---

* mogulkoc@eng.ankara.edu.tr

II. HYBRID FUNCTIONAL CALCULATIONS (HSE06)

The Heyd–Scuseria–Ernzerhof (HSE06) screened hybrid functional is employed to assess the appropriate value of the Hubbard parameter. As shown in Figs. S2 and S3 for the binary and Janus compositions, respectively, the close agreement between the band structures indicates that a Hubbard parameter of U=2 eV is suitable for all cases.

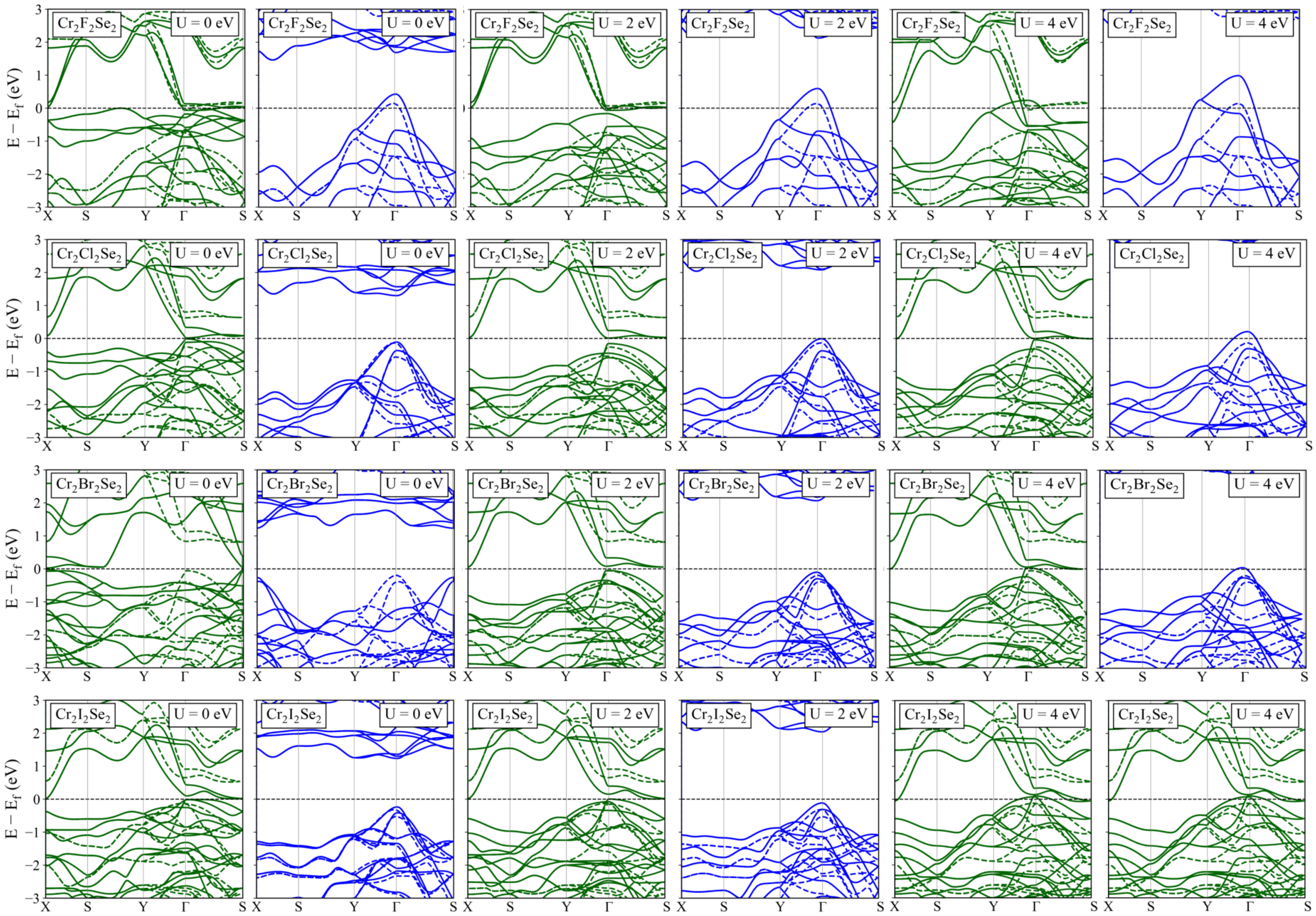

FIG. S2. Electronic band structures of binary $Cr_2X_2Se_2$ monolayer calculated using the PBE (solid lines) and HSE06 (dashed lines) methods. The green and blue curves correspond to the spin-up and spin-down channels, respectively.

III. DIFFERENT ANTIFERROMAGNETIC CONFIGURATIONS IN z-DIRECTION

Three different spin configurations are presented in FIG. S2.

IV. ANISOTROPIC HEISENBERG MODEL AND SPIN-WAVE EXCITATIONS

As Cr_2XYSe_2 monolayers show both out-of-plane and in-plane magnetic anisotropies, the details of the derivation of both are discussed below.

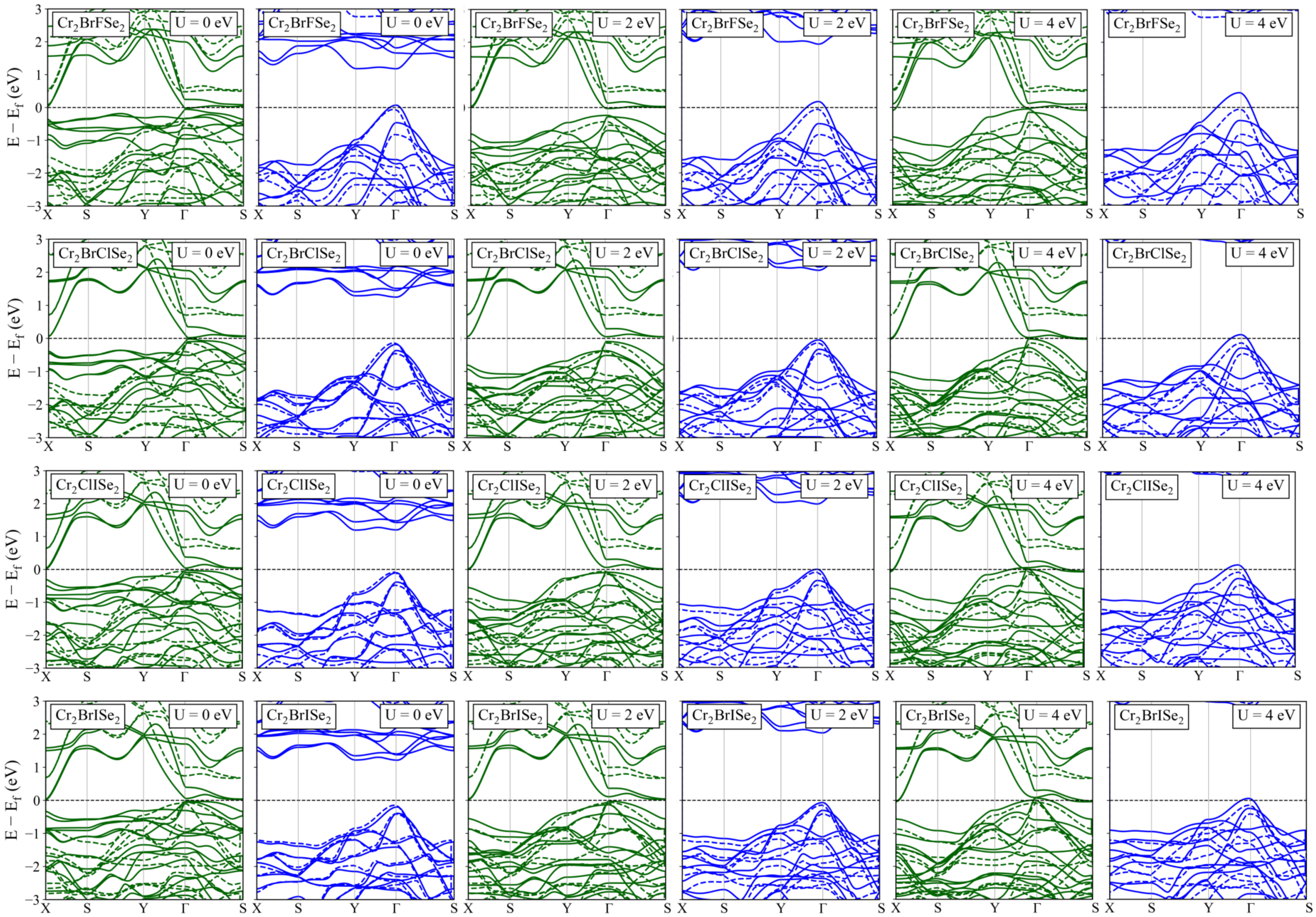

FIG. S3. Electronic band structures of Janus Cr$_2$XYSe$_2$ monolayer calculated using the PBE (solid lines) and HSE06 (dashed lines) methods. The green and blue curves correspond to the spin-up and spin-down channels, respectively.

A. Out-of-Plane Anisotropic Ferromagnets

The Hamiltonian for the anisotropic Heisenberg model for out-of-plane magnets can be written as,

$$H = -\sum_{\tau=1}^{3} J_\tau \sum_{\langle ij \rangle_\tau} \mathbf{S}_i.\mathbf{S}_j - A\sum_i (S_i^z)^2 \tag{1}$$

1. *Anisotropic Heisenberg Hamiltonian*

Each Cr atom has two first, four second, and two third nearest neighbors; accordingly, the magnetic Hamiltonian for each spin configuration can be represented

$$\begin{aligned}
E_{FM,x} &= -4J_1S^2 - 8J_2S^2 - 4J_3S^2 \\
E_{FM,z} &= -4J_1S^2 - 8J_2S^2 - 4J_3S^2 - 2AS^2 \\
E_{AFM1,z} &= -4J_1S^2 + 8J_2S^2 - 4J_3S^2 - 2AS^2 \\
E_{AFM2,z} &= 4J_1S^2 - 4J_3S^2 - 2AS^2 \\
E_{AFM3,z} &= -4J_1S^2 + 4J_3S^2 - 2AS^2
\end{aligned} \tag{2}$$

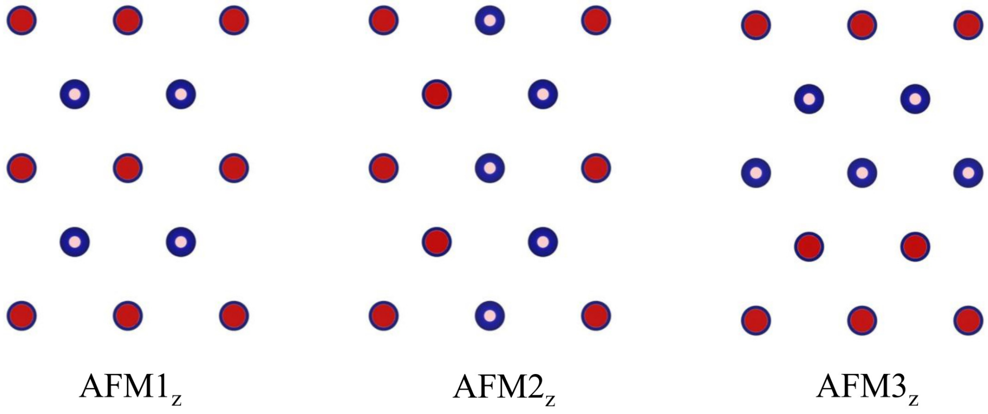

FIG. S4. Three different spin configurations in the AFM phase along the z direction, AFM1$_z$, AFM2$_z$, and AFM3$_z$.

By taking the energy differences between the magnetic configurations, the magnetic parameters are obtained as

$$\begin{aligned} J_1 &= \frac{-E_{FM,z} - E_{AFM1,z} + 2E_{AFM2,z}}{32S^2} \\ J_2 &= \frac{E_{AFM1,z} - E_{FM,z}}{32S^2} \\ J_3 &= \frac{2E_{AFM3,z} - E_{AFM1,z} - E_{FM,z}}{32S^2} \\ A &= \frac{E_{FM,x} - E_{FM,z}}{2S^2} \end{aligned} \tag{3}$$

To avoid double-counting, the exchange parameters are divided by two.

2. Holstein-Primakoff Transformation

The first-order HP transformation for the orthorhombic lattice with the out-of-plane easy axis of magnetization can be written as,

$$\begin{aligned} S_i^+ &= \sqrt{2S}a_i, \\ S_i^- &= \sqrt{2S}a_i^\dagger, \\ S_i^z &= S - a_i^\dagger a_i, \end{aligned} \tag{4}$$

for sublattice in **a** direction, and

$$\begin{aligned} S_i^+ &= \sqrt{2S}b_i, \\ S_i^- &= \sqrt{2S}b_i^\dagger, \\ S_i^z &= S - b_i^\dagger b_i. \end{aligned} \tag{5}$$

As the Hamiltonian in spin (Eq. 1) can be written as,

$$\begin{aligned} H &= H_{J_1} + H_{J_2} + H_{J_3} + H_A, \\ H_{J_1} &= -J_1 \sum_{\langle ij \rangle_1} \mathbf{S}_i.\mathbf{S}_j \\ H_{J_2} &= -J_2 \sum_{\langle ij \rangle_2} \mathbf{S}_i.\mathbf{S}_j \\ H_{J_3} &= -J_3 \sum_{\langle ij \rangle_3} \mathbf{S}_i.\mathbf{S}_j \\ H_A &= -A \sum_i (S_i^z)^2 \end{aligned} \tag{6}$$

- Transformation of H_{J_1}:

  H_{J_1} is represented as,

$$H_{J_1} = -J_1 \sum_{\langle ij \rangle_1} \frac{1}{2}(S_i^+ S_j^- + S_i^- S_j^+) + S_i^z S_j^z \tag{7}$$

After the HP transformation using Eqs. 4 and 5, the Hamiltonian in bosonic system is derived as,

$$H_{J_1} = -2SJ_1 \sum_{\langle ij \rangle_1} (a_i^\dagger a_j + b_i^\dagger b_j) - (a_i^\dagger a_i + b_i^\dagger b_i) \tag{8}$$

whereas higher-order terms of the HP transformation are neglected. We now transform the real-space operators to the reciprocal space by the Fourier transform,

$$\begin{aligned} a_i &= \frac{1}{\sqrt{N}} \sum_{\mathbf{k}} e^{i\mathbf{k}.\mathbf{r}_i} a_{\mathbf{k}} \\ b_i &= \frac{1}{\sqrt{N}} \sum_{\mathbf{k}} e^{i\mathbf{k}.\mathbf{r}_i} b_{\mathbf{k}} \end{aligned} \tag{9}$$

Here, N denotes the number of sites. Also, to continue the derivation, note that $\sum_{k,k'} e^{-i(\mathbf{k}-\mathbf{k'}).\mathbf{r_i}} = N\delta_{k,k'}$. Using the Fourier transformation,

$$H_{J_1} = 2S \sum_{\mathbf{k}} \big(J_1(\mathbf{0}) - J_1(\mathbf{k})\big)\big(a_{\mathbf{k}}^\dagger a_{\mathbf{k}} + b_{\mathbf{k}}^\dagger b_{\mathbf{k}}\big) \tag{10}$$

As each Cr atom has two first nearest neighbors along **a**, $J_1(\mathbf{k})$ is,

$$J_1(\mathbf{k}) = 4J_1 \cos{(k_x a)} \tag{11}$$

Note that as the unit cell of the monolayer consists of two Cr atoms, we multiply the structure factor by two.

- Transformation of H_{J_3}:

  By following a similar procedure as H_{J_1}, the Hamiltonin of the H_{J_3} is written as,

$$H_{J_3} = 2S \sum_{\mathbf{k}} \big(J_3(\mathbf{0}) - J_3(\mathbf{k})\big)\big(a_{\mathbf{k}}^\dagger a_{\mathbf{k}} + b_{\mathbf{k}}^\dagger b_{\mathbf{k}}\big) \tag{12}$$

As each Cr atom has two 3NN nearest neighbors along **b**, $J_1(\mathbf{k})$ is,

$$J_3(\mathbf{k}) = 4J_3 \cos{(k_y b)} \tag{13}$$

- Transformation of H_{J_2}:

  H_{J_2} is definde as,

$$H_{J_2} = -J_2 \sum_{\langle ij \rangle_2} \frac{1}{2}(S_i^+ S_j^- + S_i^- S_j^+) + S_i^z S_j^z \tag{14}$$

Applying HP transformation,

$$H_{J_2} = -2SJ_2 \sum_{\langle ij\rangle_2} (a_i^\dagger b_j + b_j^\dagger a_i) - (a_i^\dagger a_i + b_j^\dagger b_j) \tag{15}$$

Using the Fourier transformation,

$$H_{J_2} = 2S \sum_{\mathbf{k}} J_2(\mathbf{0})\big(a_{\mathbf{k}}^\dagger a_{\mathbf{k}} + b_{\mathbf{k}}^\dagger b_{\mathbf{k}}\big) - J_2(\mathbf{k})\big(a_{\mathbf{k}}^\dagger b_{\mathbf{k}} + b_{\mathbf{k}}^\dagger a_{\mathbf{k}}\big) \tag{16}$$

As each Cr atom has four first nearest neighbors in 2NN, $J_3(\mathbf{k})$ is,

$$J_2(\mathbf{k}) = 8J_2 \cos{(\frac{k_x a}{2})} \cos{(\frac{k_y b}{2})} \tag{17}$$

- Transformation of H_A:

  For the last sentence of Hamiltonian, H_A, using the HP,

  $$H_A = 2AS \sum_i (a_i^\dagger a_i + b_i^\dagger b_i) \tag{18}$$

  As a result, the Hamiltonian of the bosonic system in momentum space is derived as,

  $$H_A = 2AS \sum_{\mathbf{k}} (a_{\mathbf{k}}^\dagger a_{\mathbf{k}} + b_{\mathbf{k}}^\dagger b_{\mathbf{k}}) \tag{19}$$

The rest of the derivations are available in the main text of the Literature.

B. In-Plane Anisotropic Ferromagnets

For 2D magnets with an in-plane easy axis, the inter-site anisotropy plays a key role. In this case, the anisotropic Heisenberg Hamiltonian takes the form

$$\begin{aligned} H = &-\sum_{\tau=1}^{3} J_\tau \sum_{\langle ij\rangle_\tau} \mathbf{S}_i.\mathbf{S}_j - A\sum_i (\mathbf{S}_i.\boldsymbol{\mu})^2 \\ &- \delta \sum_{\langle ij\rangle_1} (S_i^\alpha S_j^\alpha - S_i^\beta S_j^\beta) \end{aligned} \tag{20}$$

1. Anisotropic Heisenberg Hamiltonian

Since we can define three distinct easy planes of magnetization, the magnetic parameters for each system should be considered separately.

1. Easy-plane anisotropy in the xy plane:

   In cases where the xy plane defines the easy plane of magnetization, the energy of each spin configuration based on Eq. 20,

   $$\begin{aligned} E_{FM,x} &= -4J_1S^2 - 8J_2S^2 - 4J_3S^2 - 4\delta S^2 \\ E_{FM,y} &= -4J_1S^2 - 8J_2S^2 - 4J_3S^2 + 4\delta S^2 \\ E_{FM,z} &= -4J_1S^2 - 8J_2S^2 - 4J_3S^2 - 2AS^2 \\ E_{AFM1,x} &= -4J_1S^2 + 8J_2S^2 - 4J_3S^2 - 4\delta S^2 \\ E_{AFM2,x} &= 4J_1S^2 - 4J_3S^2 + 4\delta S^2 \\ E_{AFM3,x} &= -4J_1S^2 + 4J_3S^2 - 4\delta S^2 \end{aligned} \tag{21}$$

As a result, the magnetic parameters are derived as,

$$\begin{aligned}
J_1 &= \frac{E_{FM,x} - 2E_{FM,y} - E_{AFM1,x} + 2E_{AFM2,x}}{32S^2} \\
J_2 &= \frac{E_{AFM1,x} - E_{FM,x}}{32S^2} \\
J_3 &= \frac{2E_{AFM3,x} - E_{AFM1,x-E_{FM,x}}}{32S^2} \\
A &= \frac{E_{FM,x} + E_{FM,y} - 2E_{FM,z}}{4S^2} \\
\delta &= \frac{E_{FM,y} - E_{FM,x}}{16S^2}
\end{aligned} \tag{22}$$

2. Easy-plane anisotropy in the xz plane:

With the xz plane as the easy plane of magnetization, the Heisenberg Hamiltonian in Eq. 20,

$$\begin{aligned}
E_{FM,x} &= -4J_1S^2 - 8J_2S^2 - 4J_3S^2 - 4\delta S^2 \\
E_{FM,y} &= -4J_1S^2 - 8J_2S^2 - 4J_3S^2 - 2AS^2 \\
E_{FM,z} &= -4J_1S^2 - 8J_2S^2 - 4J_3S^2 + 4\delta S^2 \\
E_{AFM1,x} &= -4J_1S^2 + 8J_2S^2 - 4J_3S^2 - 4\delta S^2 \\
E_{AFM2,x} &= 4J_1S^2 - 4J_3S^2 + 4\delta S^2 \\
E_{AFM3,x} &= -4J_1S^2 + 4J_3S^2 - 4\delta S^2
\end{aligned} \tag{23}$$

Consequently,

$$\begin{aligned}
J_1 &= \frac{E_{FM,x} - 2E_{FM,z} - E_{AFM1,x} + 2E_{AFM2,x}}{32S^2} \\
J_2 &= \frac{E_{AFM1,x} - E_{FM,x}}{32S^2} \\
J_3 &= \frac{2E_{AFM3,x} - E_{AFM1,x} - E_{FM,x}}{32S^2} \\
A &= \frac{E_{FM,x} - 2E_{FM,y} + E_{FM,z}}{4S^2} \\
\delta &= \frac{E_{FM,z} - E_{FM,x}}{16S^2}
\end{aligned} \tag{24}$$

3. Easy-plane anisotropy in the yz plane:

And with the yz plane as the easy plane, we can write the energy of each spin ordering as,

$$\begin{aligned}
E_{FM,x} &= -4J_1S^2 - 8J_2S^2 - 4J_3S^2 - 2AS^2 \\
E_{FM,y} &= -4J_1S^2 - 8J_2S^2 - 4J_3S^2 - 4\delta S^2 \\
E_{FM,z} &= -4J_1S^2 - 8J_2S^2 - 4J_3S^2 + 4\delta S^2 \\
E_{AFM1,z} &= -4J_1S^2 + 8J_2S^2 - 4J_3S^2 + 4\delta S^2 \\
E_{AFM2,z} &= 4J_1S^2 - 4J_3S^2 - 4\delta S^2 \\
E_{AFM3,z} &= -4J_1S^2 + 4J_3S^2 + 4\delta S^2
\end{aligned} \tag{25}$$

Accordingly,

$$\begin{aligned}
J_1 &= \frac{E_{FM,z} - 2E_{FM,y} - E_{AFM1,z} + 2E_{AFM2,z}}{32S^2} \\
J_2 &= \frac{E_{AFM1,z} - E_{FM,z}}{32S^2} \\
J_3 &= \frac{2E_{AFM3,z} - E_{AFM1,z} - E_{FM,z}}{32S^2} \\
A &= \frac{E_{FM,y} - 2E_{FM,x} + E_{FM,z}}{4S^2} \\
\delta &= \frac{E_{FM,z} - E_{FM,y}}{16S^2}
\end{aligned} \tag{26}$$

2. Holstein-Primakoff Transformation

For in-plane magnets, the HP transformations can be written for the sublattice in the **a** direction,

$$\begin{aligned}
&S_i^+ \sqrt{2S} a_i^\dagger, \\
&S_i^- = \sqrt{2S} a_i, \\
&S_i^{x,y} = a_i^\dagger a_i - S,
\end{aligned} \tag{27}$$

and for sublattice in **b** direction,

$$\begin{aligned}
S_i^+ &= \sqrt{2S} b_i^\dagger, \\
S_i^- &= \sqrt{2S} b_i, \\
S_i^{x,y} &= b_i^\dagger b_i - S.
\end{aligned} \tag{28}$$

The Hamiltonian of Eq. 20 can be written for xy as the easy plane of magnetization,

$$\begin{aligned}
H &= H_{J_1} + H_{J_2} + H_{J_3} + H_A, \\
H_{J_1} &= -J_1 \sum_{\langle ij \rangle_1} \mathbf{S}_i . \mathbf{S}_j \\
H_{J_2} &= -J_2 \sum_{\langle ij \rangle_2} \mathbf{S}_i . \mathbf{S}_j \\
H_{J_3} &= -J_3 \sum_{\langle ij \rangle_3} \mathbf{S}_i . \mathbf{S}_j \\
H_A &= -A \sum_i (S_i^z)^2 \\
H_\delta &= -\delta \sum_{\langle ij \rangle_1} (S_i^x S_j^x - S_i^y S_j^y)
\end{aligned} \tag{29}$$

Now, to derive the magnon dispersion, we use the HP transformation on each sentence of the Hamiltonian.

- Transformation of H_{J_1}, H_{J_2}, and H_{J_3}

  H_{J_1} is defined as,

$$H_{J_1} = -J_1 \sum_{\langle ij \rangle_1} \frac{1}{2}(S_i^+ S_j^- + S_i^- S_j^+) + S_i^x S_j^x \tag{30}$$

We obtain the same exchange terms in the Hamiltonian as in the out-of-plane case, given in Eqs. 10, 16, and 12.

- Transformation of H_A

  For the single-ion anisotropy term H_A, using the relation $S_i^x = -S_i^z \pm iS_i^y$, and applying the HP transformation,

$$H_A = -\frac{SA}{2}\sum_i (a_i^\dagger a_i^\dagger + a_i a_i + 2a_i^\dagger a_i) + (b_i^\dagger b_i^\dagger + b_i b_i + 2b_i^\dagger b_i) \tag{31}$$

  After the Fourier transformation,

$$H_A = -\frac{SA}{2}\sum_{\mathbf{k}} (a_{\mathbf{k}}^\dagger a_{-\mathbf{k}}^\dagger + a_{\mathbf{k}} a_{-\mathbf{k}} + 2a_{\mathbf{k}}^\dagger a_{\mathbf{k}}) + (b_{\mathbf{k}}^\dagger b_{-\mathbf{k}}^\dagger + b_{\mathbf{k}} b_{-\mathbf{k}} + 2b_{\mathbf{k}}^\dagger b_{\mathbf{k}}) \tag{32}$$

- Transformation of H_δ

  To transform the inter-site anisotropy from the spin to the boson space,

$$\begin{aligned} H_\delta &= H_\delta(1) + H_\delta(2) \\ H_\delta(1) &= -\delta \sum_{\langle ij\rangle_1} S_i^x S_j^x \\ H_\delta(2) &= \delta \sum_{\langle ij\rangle_1} S_i^y S_j^y \end{aligned} \tag{33}$$

  Using the HP transformation into $H_\delta(1)$,

$$H_\delta(1) = 2\delta S \sum_{\langle ij\rangle_1} (a_i^\dagger a_i + b_i^\dagger b_i) \tag{34}$$

  As a result,

$$H_\delta(1) = 2S\sum_{\mathbf{k}} \delta(\mathbf{0})(a_{\mathbf{k}}^\dagger a_{\mathbf{k}} + b_{\mathbf{k}}^\dagger b_{\mathbf{k}}) \tag{35}$$

  and for $H_\delta(2)$, as the result of applying HP transformation,

$$H_\delta(2) = -\frac{S\delta}{2}\sum_{\langle ij\rangle_1} (a_i^\dagger a_j^\dagger + a_i a_j - 2a_i^\dagger a_j) + (b_i^\dagger b_j^\dagger + b_i b_j - 2b_i^\dagger b_j) \tag{36}$$

  And finally, by applying the Fourier transformation,

$$H_\delta(2) = -\frac{S}{2}\sum_{\mathbf{k}} \delta(\mathbf{k})(a_{\mathbf{k}}^\dagger a_{-\mathbf{k}}^\dagger + a_{\mathbf{k}} a_{-\mathbf{k}} - 2a_{\mathbf{k}}^\dagger a_{\mathbf{k}}) + (b_{\mathbf{k}}^\dagger b_{-\mathbf{k}}^\dagger + b_{\mathbf{k}} b_{-\mathbf{k}} - 2b_{\mathbf{k}}^\dagger b_{\mathbf{k}}) \tag{37}$$

  And H_δ is derived as,

$$H_\delta = S\sum_{\mathbf{k}} \big(2\delta(\mathbf{k}) + \delta(\mathbf{0})\big)\big(a_{\mathbf{k}}^\dagger a_{\mathbf{k}} + b_{\mathbf{k}}^\dagger b_{\mathbf{k}}\big) - \frac{1}{2}\delta(\mathbf{k})\big(a_{\mathbf{k}}^\dagger a_{-\mathbf{k}}^\dagger + a_{\mathbf{k}} a_{-\mathbf{k}} + b_{\mathbf{k}}^\dagger b_{-\mathbf{k}}^\dagger + b_{\mathbf{k}} b_{-\mathbf{k}}\big) \tag{38}$$

  Where,

$$\delta(\mathbf{k}) = 4\delta\cos(k_x a) \tag{39}$$

V. ELECTRONIC PROPERTIES

A. Cr–Cr bond distances as a function of Hubbard U

The bond distance for the first, second, and third Cr-Cr nearest neighbors for binary and Janus composition are presented in Tables. I and II, respectively.

TABLE I. Calculated Cr–Cr bond distances (in Å) as a function of Hubbard U (eV) for binary $Cr_2X_2Se_2$ monolayers.

Material	U (eV)	Cr–Cr (1st)	Cr–Cr (2nd)	Cr–Cr (3rd)
$Cr_2F_2Se_2$	0	3.30	3.77	5.09
	2	3.31	3.80	5.14
	4	3.26	3.86	5.28
$Cr_2Cl_2Se_2$	0	3.53	3.81	5.05
	2	3.56	3.84	5.11
	4	3.58	3.88	5.18
$Cr_2Br_2Se_2$	0	3.64	3.82	5.04
	2	3.66	3.85	5.10
	4	3.69	3.88	5.16
$Cr_2I_2Se_2$	0	3.80	3.83	5.01
	2	3.83	3.86	5.08
	4	3.86	3.90	5.15

TABLE II. Calculated Cr–Cr bond distances (in Å) as a function of Hubbard U (eV) for Janus Cr_2XYSe_2 monolayers.

Material	U (eV)	Cr–Cr (1st)	Cr–Cr (2nd)	Cr–Cr (3rd)
Cr_2BrFSe_2	0	3.48	3.82	5.11
	2	3.48	3.84	5.15
	4	3.49	3.86	5.19
$Cr_2BrClSe_2$	0	3.58	3.81	5.04
	2	3.61	3.84	5.10
	4	3.63	3.88	5.17
Cr_2ClISe_2	0	3.66	3.82	5.03
	2	3.69	3.85	5.10
	4	3.70	3.89	5.17
Cr_2BrISe_2	0	3.72	3.82	5.02
	2	3.74	3.85	5.09
	4	3.77	3.89	5.16

B. Bader Charge of Different Compositions of Cr_2XYSe_2

The Bader charge of different composition are presented in Table. III and IV for binary and Janus monolayers. The Bader charge analysis at U = 2 eV reveals systematic charge transfer from Cr to the surrounding halogen and Se atoms in both binary and Janus monolayers. In binary $Cr_2X_2Se_2$ systems, the Cr charge decreases monotonically from F (1.30 $|e|$) to I (1.04 $|e|$), following the trend of halogen electronegativity, indicating reduced bond ionicity for heavier halogens. In Janus Cr_2XYSe_2 structures, the Cr charge remains intermediate ($\sim$1.12-1.18 $|e|$), while the more electronegative halogen yields a more negative charge, leading to asymmetric charge distribution across the two sides. Meanwhile, the Se charge varies only slightly in both cases, suggesting that halogen substitution primarily tunes the Cr-X bonding character and enhances structural polarity in Janus systems.

TABLE III. Calculated Bader charge (in $|e|$) of Cr, halogen X, and Se atoms in binary $Cr_2X_2Se_2$ monolayers, at U=2 eV.

Material	Cr ($|e|$)	X ($|e|$)	Se ($|e|$)
$Cr_2F_2Se_2$	1.30	-0.70	-0.60
$Cr_2Cl_2Se_2$	1.20	-0.57	-0.63
$Cr_2Br_2Se_2$	1.11	-0.47	-0.64
$Cr_2I_2Se_2$	1.04	-0.36	-0.67

C. Partial Density of States (PDOS) of Cr_2XYSe_2

The *d*-orbital nature of the Cr atom is confirmed by plotting the partial density of states (PDOS) of binary and Janus composition as depicted in Figs. S5 and S6. Due to the low-symmetry orthorhombic crystal structure and the

TABLE IV. Calculated Bader charge (in $|e|$) of Cr, halogen X, Y, and Se atoms in Janus Cr_2XYSe_2 monolayers, at U=2 eV.

Material	Cr ($|e|$)	X ($|e|$)	Y ($|e|$)	Se ($|e|$)
Cr_2BrFSe_2	1.13	-0.47	-0.71	-0.62
$Cr_2BrClSe_2$	1.12	-0.48	-0.54	-0.63
Cr_2ClISe_2	1.18	-0.56	-0.37	-0.64
Cr_2BrISe_2	1.12	-0.47	-0.36	-0.65

strong hybridization between Cr d-orbitals and ligand p states, the Cr $3d$ bands become fully nondegenerate. As a result, the conventional crystal-field splitting with well-defined t_{2g} and e_g splitting is no longer predictable.

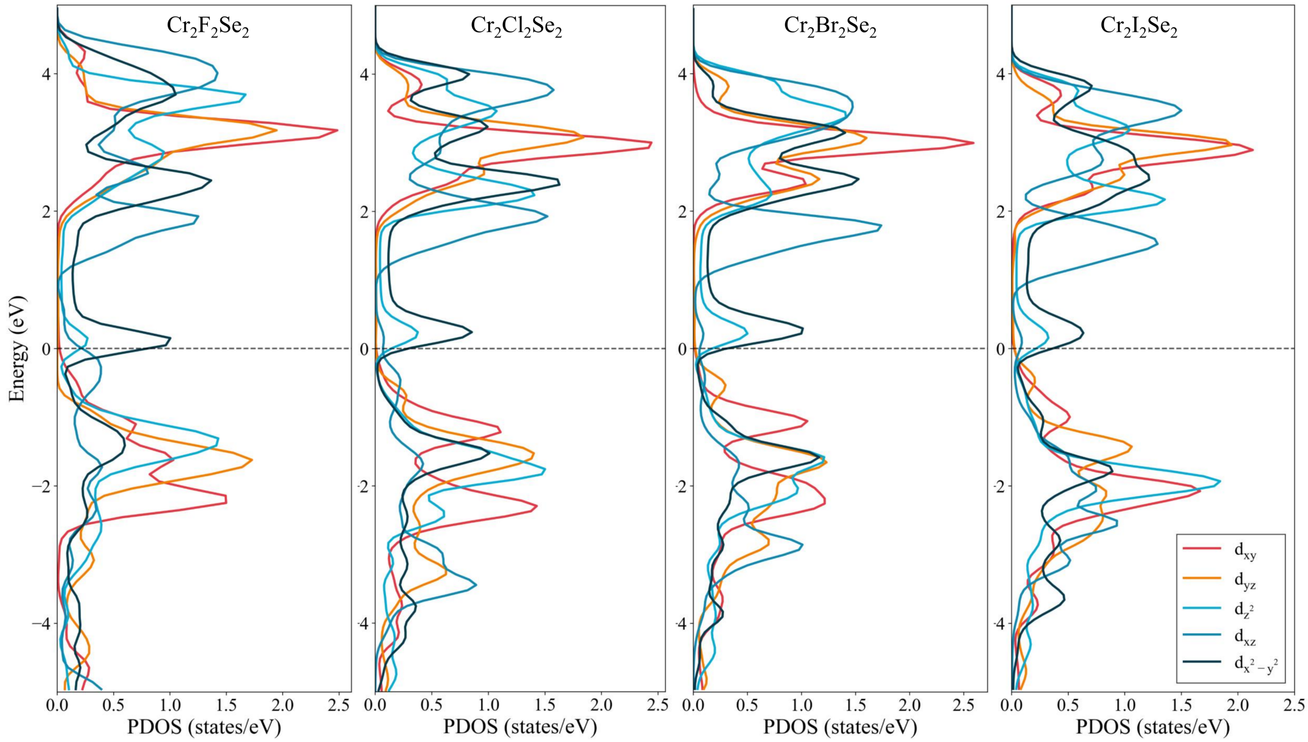

FIG. S5. partial density of states (PDOS) calculated for binary-$Cr_2X_2Se_2$ monolayer with U = 2 eV.

D. Local Magnetic Moment

The local magnetic moment per Cr atom is presented in Table. V. The results indicate that halogen substitution does not lead to any significant variation in the Cr magnetic moment.

E. Orbital Magnetic Moments

The largest orbital moments calculated along the $L_\perp$ and $L_\parallel$ directions are reported in Tables. VI and VII for binary and Janus compositions. It is clear that $|L_\parallel| > |L_\perp|$ for the in-plane magnetization configuration. Importantly, the opposite condition, $|L_\parallel| < |L_\perp|$, is not observed even for the out-of-plane case in our compositions. Although $|L_\perp|$ increases with increasing U, its magnitude remains smaller than $|L_\parallel|$ for all considered values of U for out-of-plane systems. Consequently, the orbital moment anisotropy consistently favors the in-plane direction. However, since magnetocrystalline anisotropy energy is determined by the spin–orbit coupling interactions and not only by the magnitude of orbital moments, the magnetic easy axis can still switch to the out-of-plane direction despite the absence of orbital moment reversal.

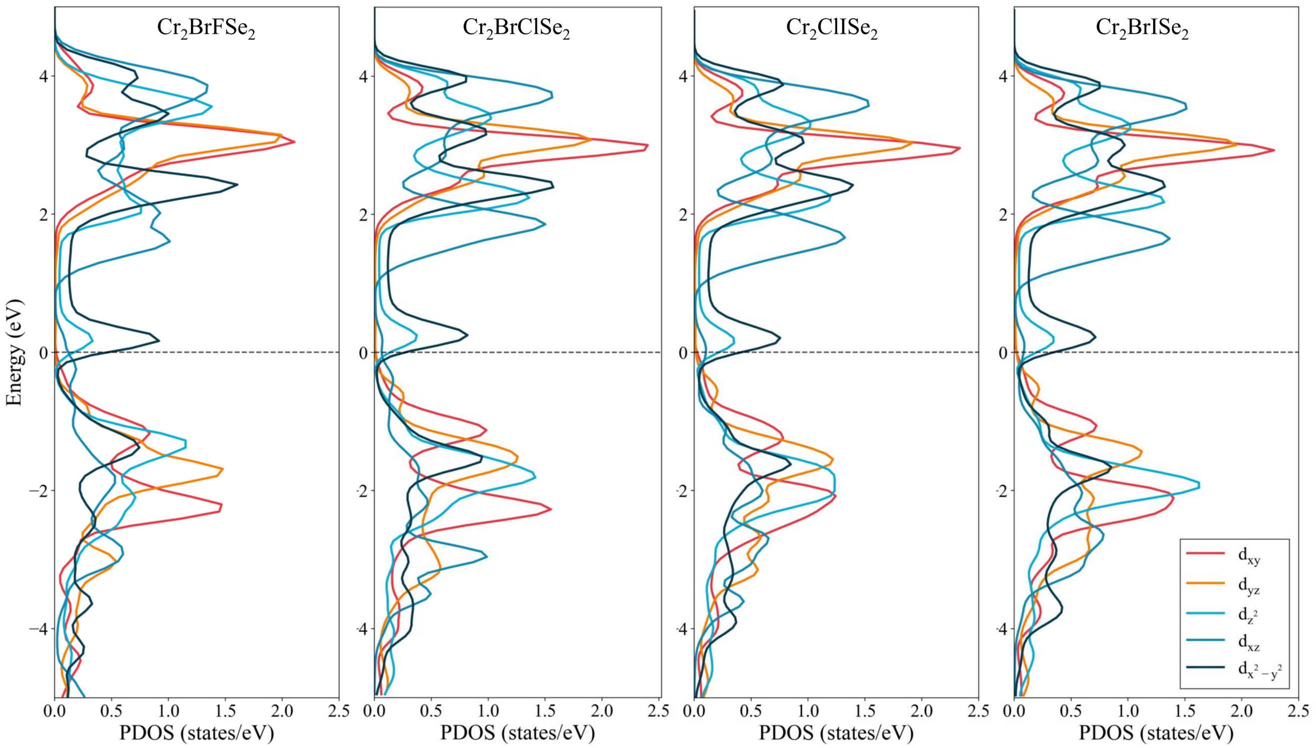

FIG. S6. Partial density of states (PDOS) calculated for Janus-Cr_2XYSe_2 monolayer with U = 2 eV.

TABLE V. Calculated local magnetic moment per Cr atom (μ_B) in binary $Cr_2X_2Se_2$ and Janus Cr_2XYSe_2 monolayers at $U = 2$ eV.

Material	m_{Cr} (μ_B)
$Cr_2F_2Se_2$	3.15
$Cr_2Cl_2Se_2$	2.99
$Cr_2Br_2Se_2$	2.97
$Cr_2I_2Se_2$	3.00
Cr_2BrFSe_2	3.05
$Cr_2BrClSe_2$	2.98
Cr_2ClISe_2	3.00
Cr_2BrISe_2	2.99

VI. SPIN-POLARIZED ELECTRONIC BAND STRUCTURES

The electronic spin-polarized band structure demonstrates that by including on-site Coulomb energy, the electronic phase can be transformed from a semiconductor to a metallic phase.

VII. AB INITIO MOLECULAR DYNAMICS (AIMD) SIMULATIONS

The thermal stability of binary and Janus Cr_2XYSe_2 monolayers is investigated using the AIMD simulations carried out with the NVT ensemble and employing the Andersen thermostat. The corresponding fluctuations of the total energy and the structure snapshots taken every 2 ps are shown in Fig. S8 and S9 for binary and Janus chemical compositions, respectively. One can see that the atomic structure remains stable and essentially flat at the transition temperature corresponding to U = 2 eV. Some distortions from the perfect hexagonal lattice are not large and can be related to thermal fluctuations. The maximum of the averaged total energy fluctuation is around 40 meV/atom for the Janus compositions. This allows us to confirm the thermal stability of the monolayer at the reported transition temperature.

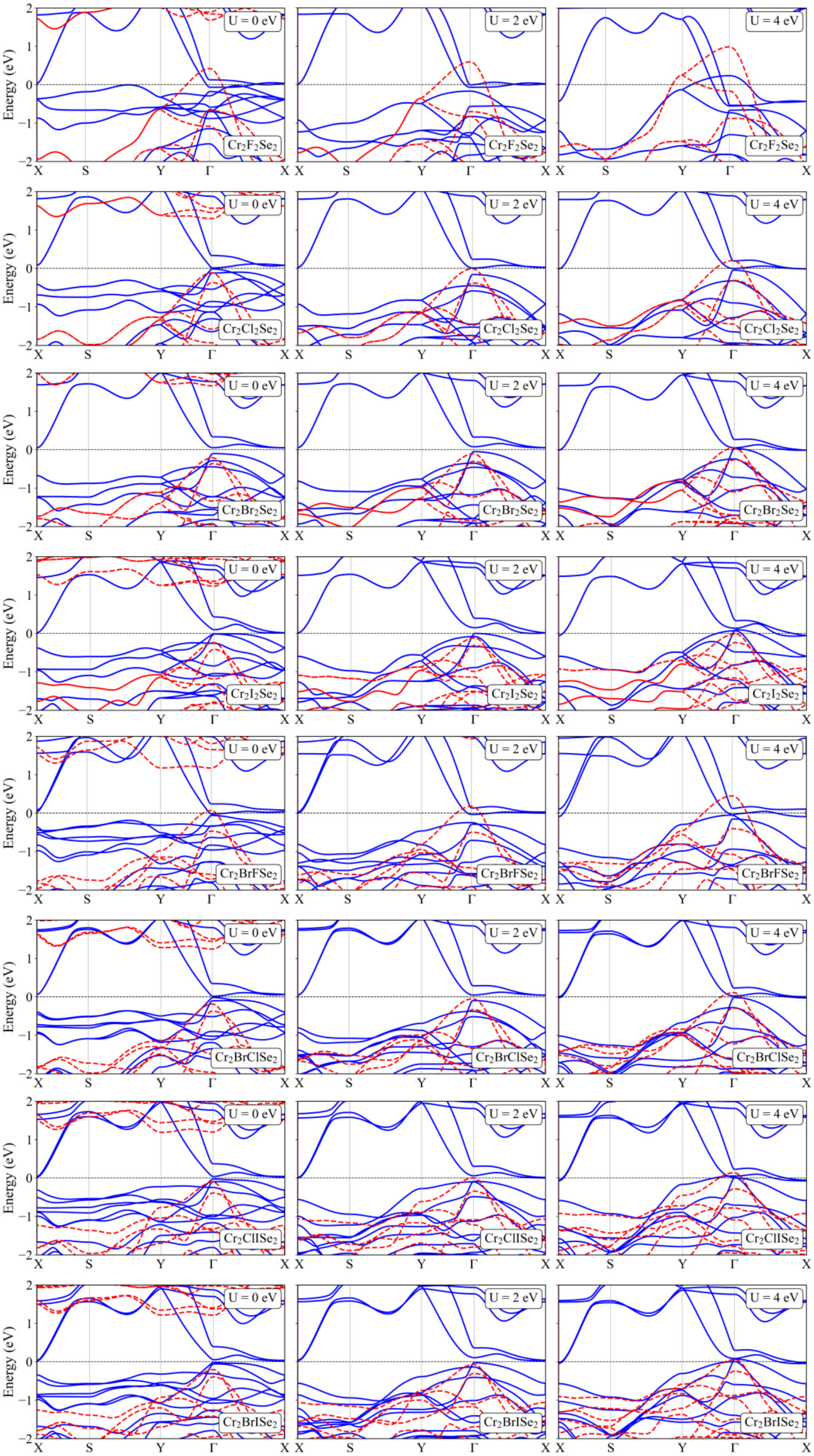

FIG. S7. Spin-polarized electronic band structures for U = 0, 2 and 4 eV for 2D-Cr_2XYSe_2. The blue and red colors belong to the up and down spin channels, respectively.

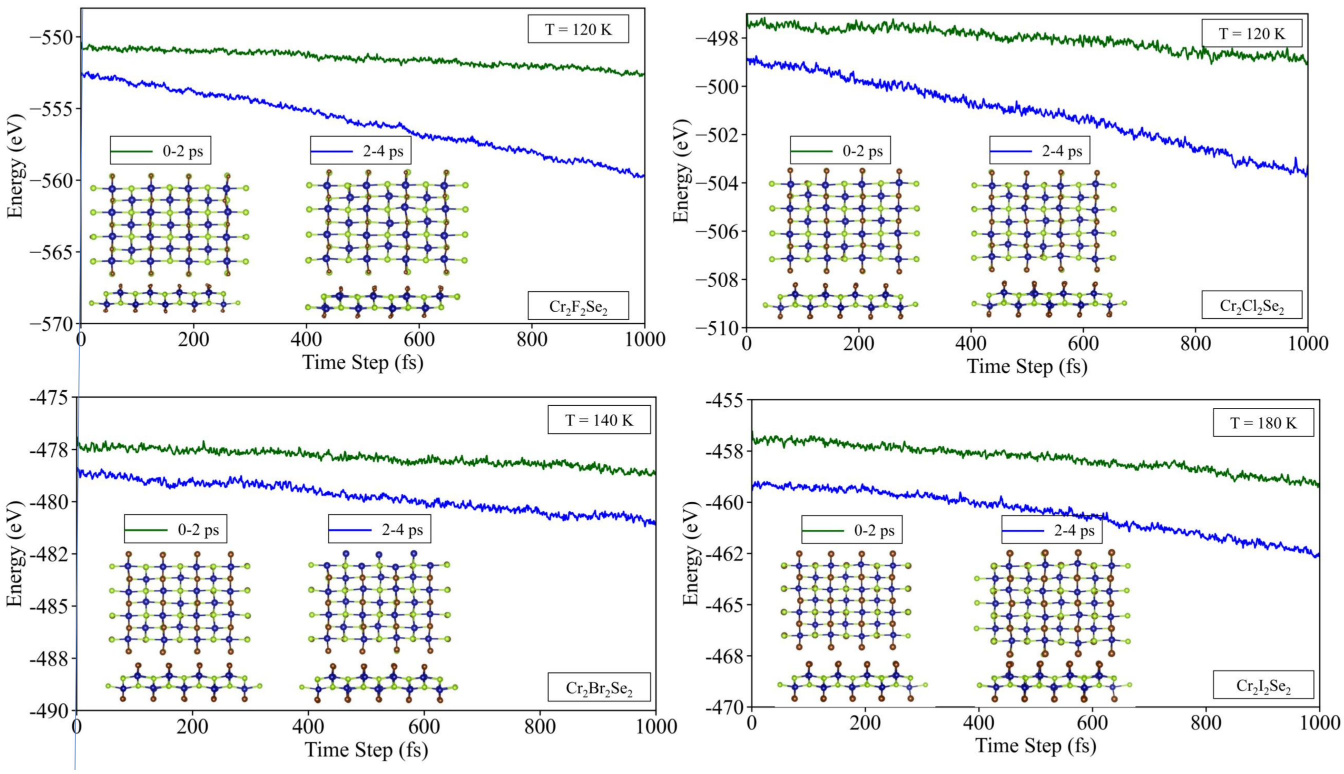

FIG. S8. Total energy obtained from the AIMD simulation over 4 ps in the NVT ensemble for binary $Cr_2X_2Se_2$. The temperature is selected in accordance with the transition temperature that corresponds to U = 2 eV.

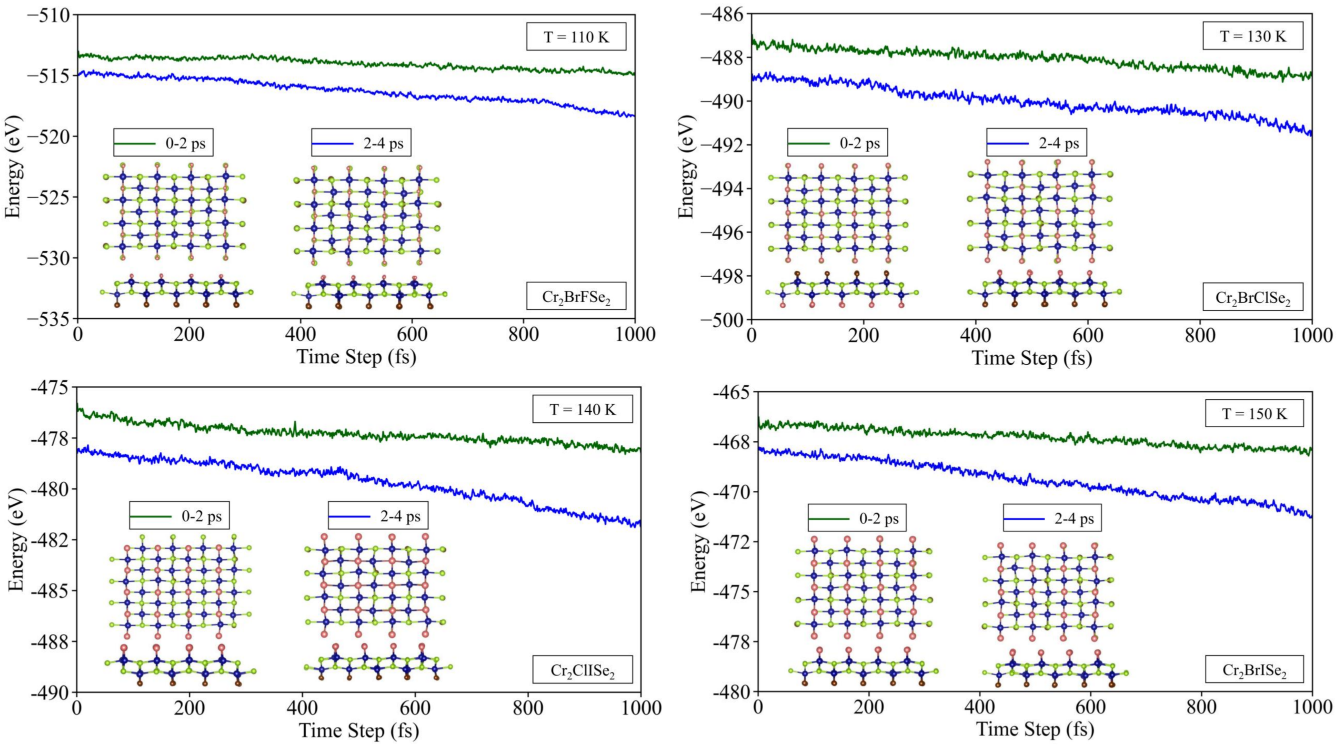

FIG. S9. Total energy reached from the AIMD simulation performed over a period of 4 ps with the NVT ensemble for Janus Cr_2XYSe_2. The temperature is selected in accordance with the transition temperature that corresponds to U = 2 eV.

TABLE VI. Maximum in-plane ($L_{\parallel}^{\max}$) and out-of-plane ($L_{\perp}^{\max}$) orbital magnetic moments (in μ_B) as a function of Hubbard U (eV) for binary $Cr_2X_2Se_2$ monolayers.

Material	U (eV)	$L_{\parallel}^{\max}$ (μ_B)	$L_{\perp}^{\max}$ (μ_B)
$Cr_2F_2Se_2$	0	0.043	0.036
	1	0.041	0.038
	2	0.045	0.041
	3	0.048	0.044
	4	0.058	0.039
$Cr_2Cl_2Se_2$	0	0.036	0.024
	1	0.040	0.027
	2	0.044	0.030
	3	0.049	0.033
	4	0.053	0.035
$Cr_2Br_2Se_2$	0	0.020	0.006
	1	0.025	0.011
	2	0.031	0.015
	3	0.037	0.020
	4	0.043	0.024
$Cr_2I_2Se_2$	0	0.026	0.015
	1	0.006	0.007
	2	0.017	0.004
	3	0.028	0.015
	4	0.039	0.026

TABLE VII. Maximum in-plane ($L_{\parallel}^{\max}$) and out-of-plane ($L_{\perp}^{\max}$) orbital magnetic moments (in μ_B) as a function of Hubbard U (eV) for Janus Cr_2XYSe_2 monolayers.

Material	U (eV)	$L_{\parallel}^{\max}$ (μ_B)	$L_{\perp}^{\max}$ (μ_B)
Cr_2BrFSe_2	0	0.029	0.029
	1	0.033	0.023
	2	0.037	0.027
	3	0.042	0.031
	4	0.046	0.035
$Cr_2BrClSe_2$	0	0.028	0.015
	1	0.032	0.019
	2	0.037	0.023
	3	0.043	0.026
	4	0.048	0.029
Cr_2ClISe_2	0	0.016	0.006
	1	0.021	0.012
	2	0.028	0.018
	3	0.035	0.025
	4	0.042	0.031
Cr_2BrISe_2	0	0.009	0.002
	1	0.015	0.002
	2	0.023	0.010
	3	0.031	0.018
	4	0.040	0.025

VIII. ORBITAL-PROJECTED SOC AND MAE

To describe the orbital origin of the easy-axis reorientation, we consider the perturbative contribution of the SOC Hamiltonian, $H_{\mathrm{SOC}} = \lambda\,\mathbf{L}\cdot\mathbf{S}$, where λ represents the SOC strength. The contribution of each SOC channel to magnetic anisotropy energy (MAE) is determined,

$$MAE = \lambda^2 \sum_{o^+,u^+} \frac{|\langle o^+|\hat{L}_z|u^+\rangle|^2 - |\langle o^+|\hat{L}_x|u^+\rangle|^2}{\varepsilon_{u^+} - \varepsilon_{o^+}} - \lambda^2 \sum_{o^-,u^+} \frac{|\langle o^-|\hat{L}_z|u^+\rangle|^2 - |\langle o^-|\hat{L}_x|u^+\rangle|^2}{\varepsilon_{u^+} - \varepsilon_{o^-}} \tag{40}$$

Here, λ denotes the SOC strength, with the $+$ and $-$ signs corresponding to the spin-up and spin-down channels, respectively. The quantities ε_u and ε_o represent the energies of the unoccupied and occupied states. The angular momentum operators $\hat{L}_z$ and $\hat{L}_x$ are driven by the out-of-plane and in-plane magnetization directions, respectively. The orbital-projected SOC energy difference, ΔE_{SOC}, shown in Figs. S10-S14, is determined by the difference between the SOC energies for in-plane (E_x^{SOC}) and out-of-plane (E_z^{SOC}) magnetization directions The orbital-projected SOC energy difference is determined by the difference between the SOC energies for in-plane (E_x^{SOC}) and out-of-plane (E_z^{SOC}) magnetization directions. We have presented the issue of the magnetic easy axis changing with the variation of the Hubbard parameter for $\mathrm{Cr_2F_2Se_2}$, $\mathrm{Cr_2I_2Se_2}$, $\mathrm{Cr_2BrFSe_2}$, $\mathrm{Cr_2ClISe_2}$, and $\mathrm{Cr_2BrISe_2}$, as shown in Figs. S10 to S14, respectively.

By varying the Hubbard U parameter, the orbital-resolved spin-orbit coupling (SOC) contributions are significantly modified, leading to a reorientation of the magnetic easy axis, as discussed below. As shown in Fig. S10, for $\mathrm{Cr_2F_2Se_2}$ at U = 0 eV, the dominant SOC matrix elements arise from the hybridization between the Cr $d_{x^2-y^2}$ orbital with the d_{xy} and d_{yz} states, together with the Se p_x-p_y orbitals, favoring in-plane magnetic anisotropy. When U increases to 1 eV, the leading contributions shift to the Cr d_{xy}-d_{yz} and d_{xz}-d_{z^2} channels, along with the Se p_x-p_z interaction, stabilizing an out-of-plane magnetization.

For $\mathrm{Cr_2I_2Se_2}$ (Fig. S11), the larger electronegativity and strong SOC strength of iodine substantially influence the magnetic anisotropy. With increasing U, the dominant iodine p-orbital coupling changes from p_y-p_z to p_x-p_y, accompanied by a redistribution of the Cr d-orbital contributions. This orbital reorganization is responsible for the modification of the easy axis. In the Janus compositions, the Se p orbitals also play a non-negligible role in determining the anisotropy. As illustrated in Fig. S12, at U = 3 eV the in-plane anisotropy is mainly governed by the Se p_x-p_z coupling and the Cr d_{xy}-d_{yz} and d_{xz}-d_{z^2} interactions. In contrast, at U = 4 eV, the Br p_x-p_y channel becomes dominant, together with additional contributions from Se p_x-p_z and Cr d-orbital hybridizations, reflecting the enhanced localization of Cr d states with increasing U. Similarly, for $\mathrm{Cr_2ClISe_2}$ and $\mathrm{Cr_2BrISe_2}$ (Figs. S13-S14), the iodine p orbitals provide the leading contribution to the magnetocrystalline anisotropy. As U increases, the dominant coupling shifts from p_y–p_z to p_x–p_y, accompanied by a redistribution of the Cr d-orbital matrix elements.

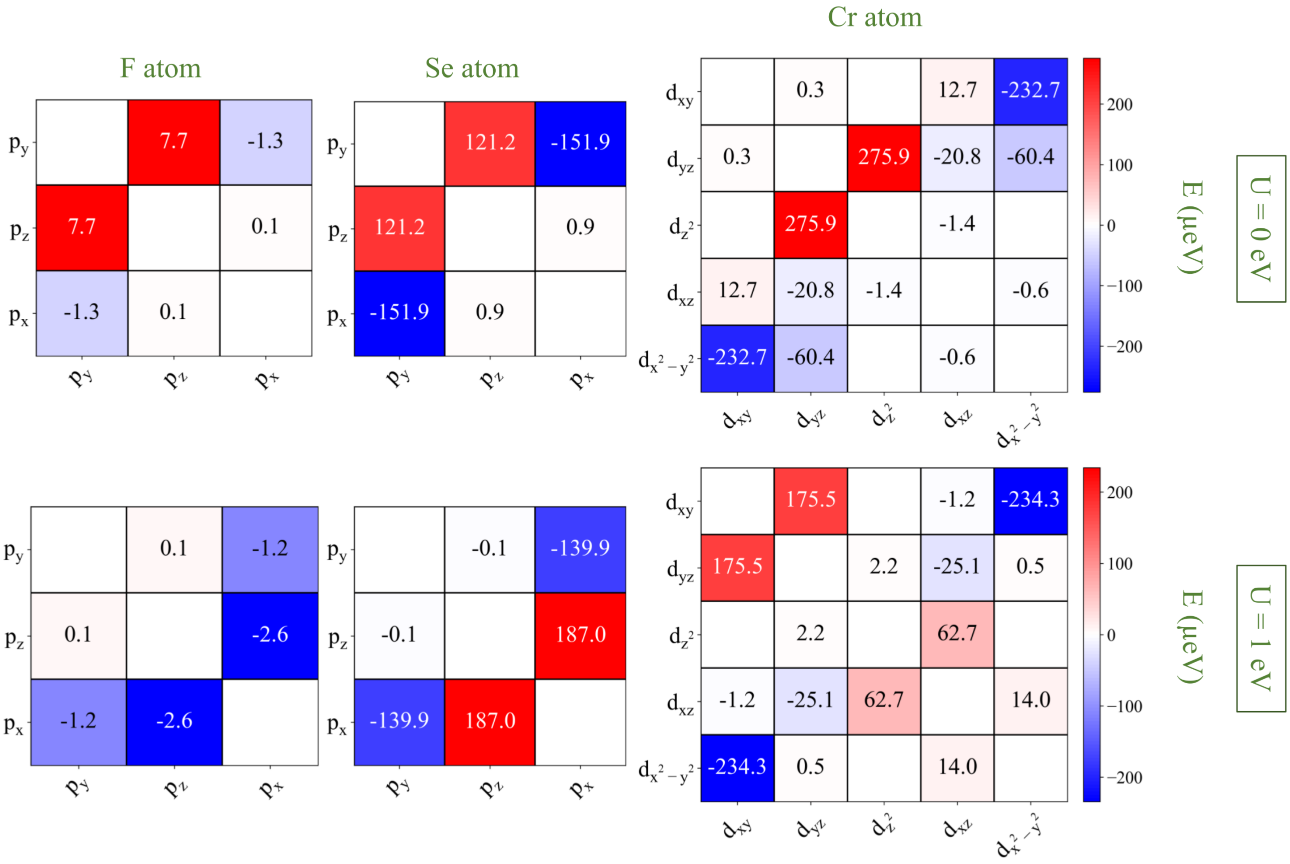

FIG. S10. Orbital-projected contributions of spin–orbit coupling (SOC) from Cr-3d, F-2p, and Se-4p states to the magnetocrystalline anisotropy energy (MAE) for $Cr_2F_2Se_2$ monolayer at U = 0 and 1 eV, where a change in the magnetic easy axis is observed.

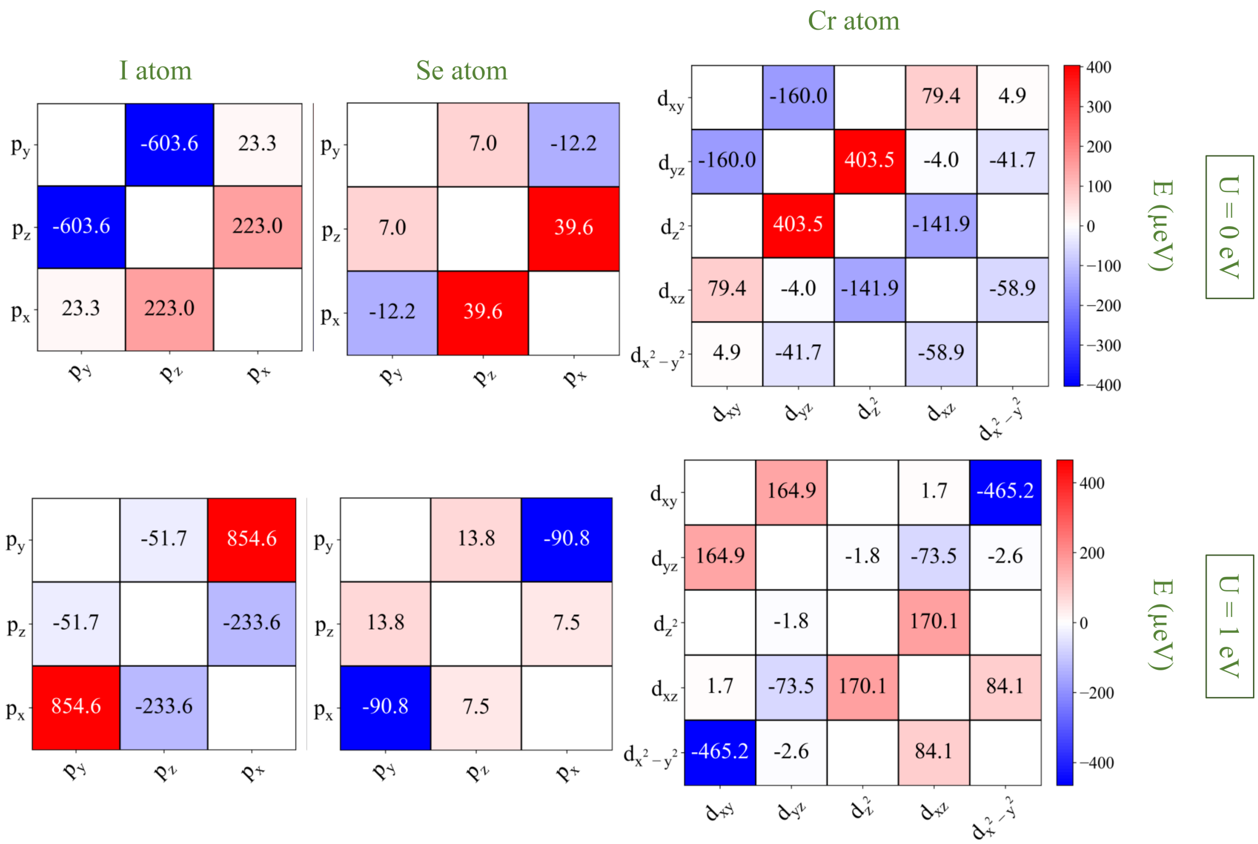

FIG. S11. Orbital-projected contributions of spin–orbit coupling (SOC) from Cr-3d, I-2p, and Se-4p states to the magnetocrystalline anisotropy energy (MAE) for $Cr_2I_2Se_2$ at $U = 0$ and 1 eV, where a change in the magnetic easy axis is observed.

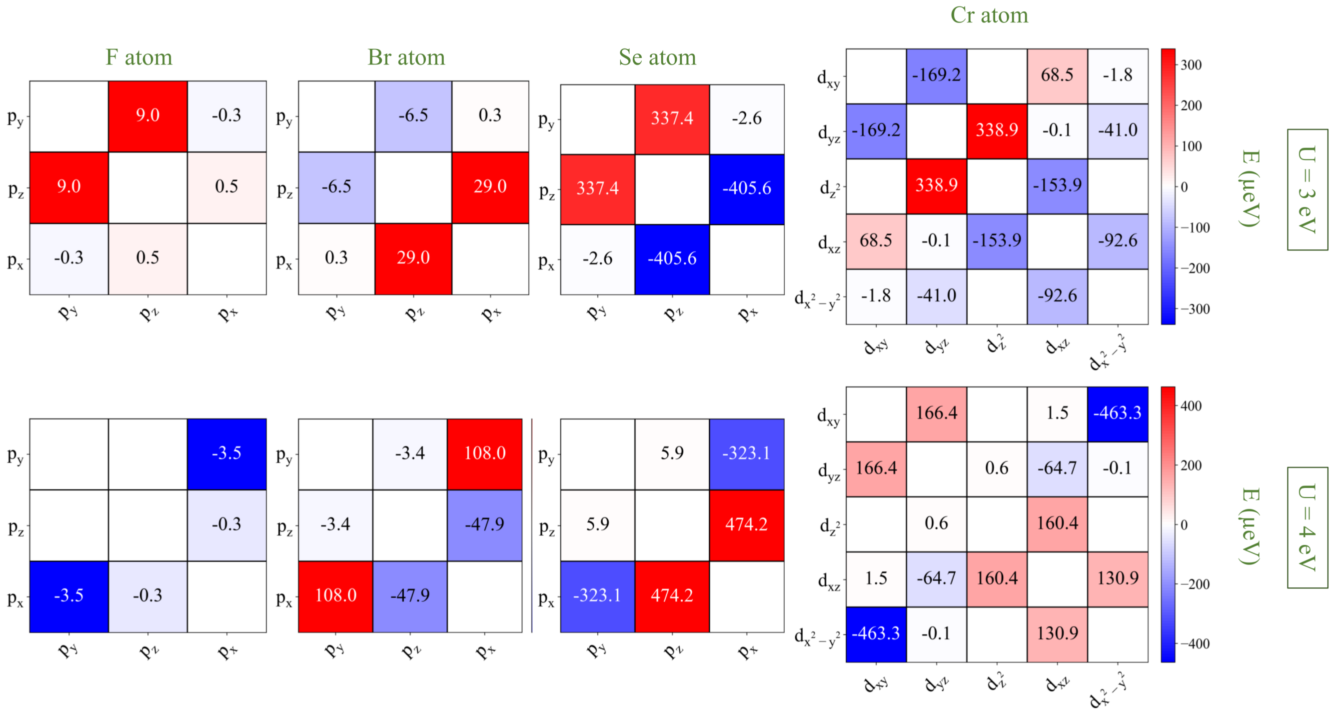

FIG. S12. Orbital-projected contributions of spin–orbit coupling (SOC) from Cr-3d, F-2p, Br-2p, and Se-4p states to the magnetocrystalline anisotropy energy (MAE) for Cr_2BrFSe_2 at U = 3 and 4 eV, where a change in the magnetic easy axis is observed.

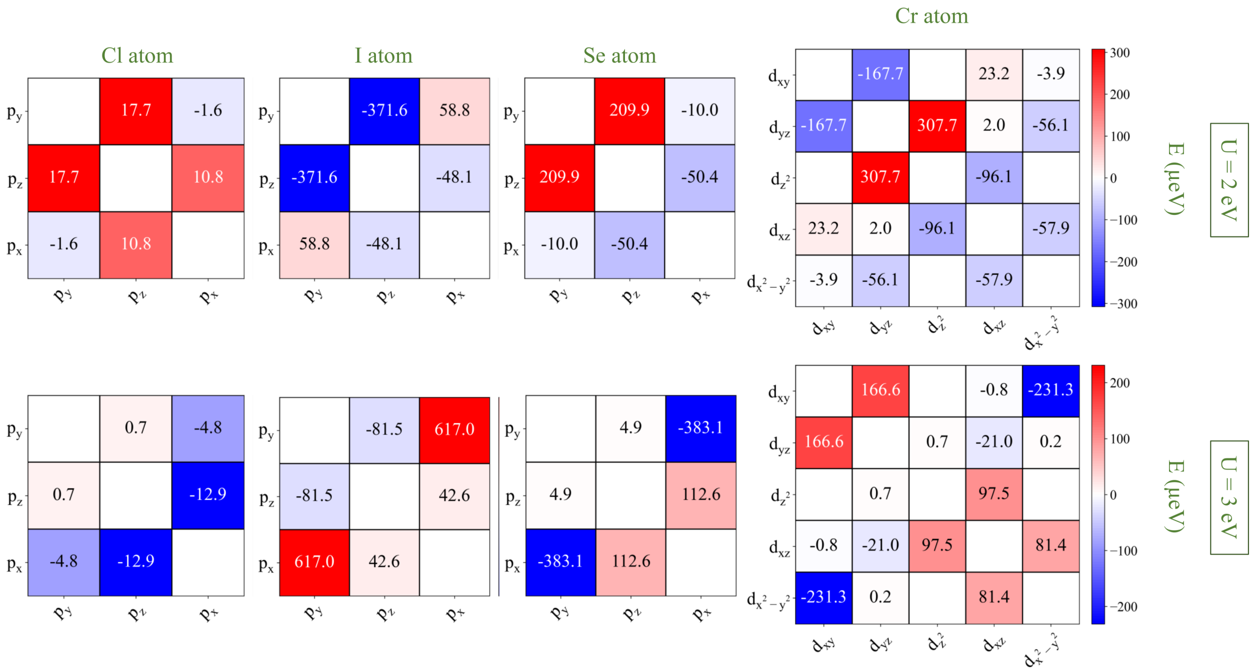

FIG. S13. Orbital-projected contributions of spin–orbit coupling (SOC) from Cr-3d, Cl-2p, I-2p, and Se-4p states to the magnetocrystalline anisotropy energy (MAE) for Cr_2ClISe_2 at U = 2 and 3 eV, where a change in the magnetic easy axis is observed.

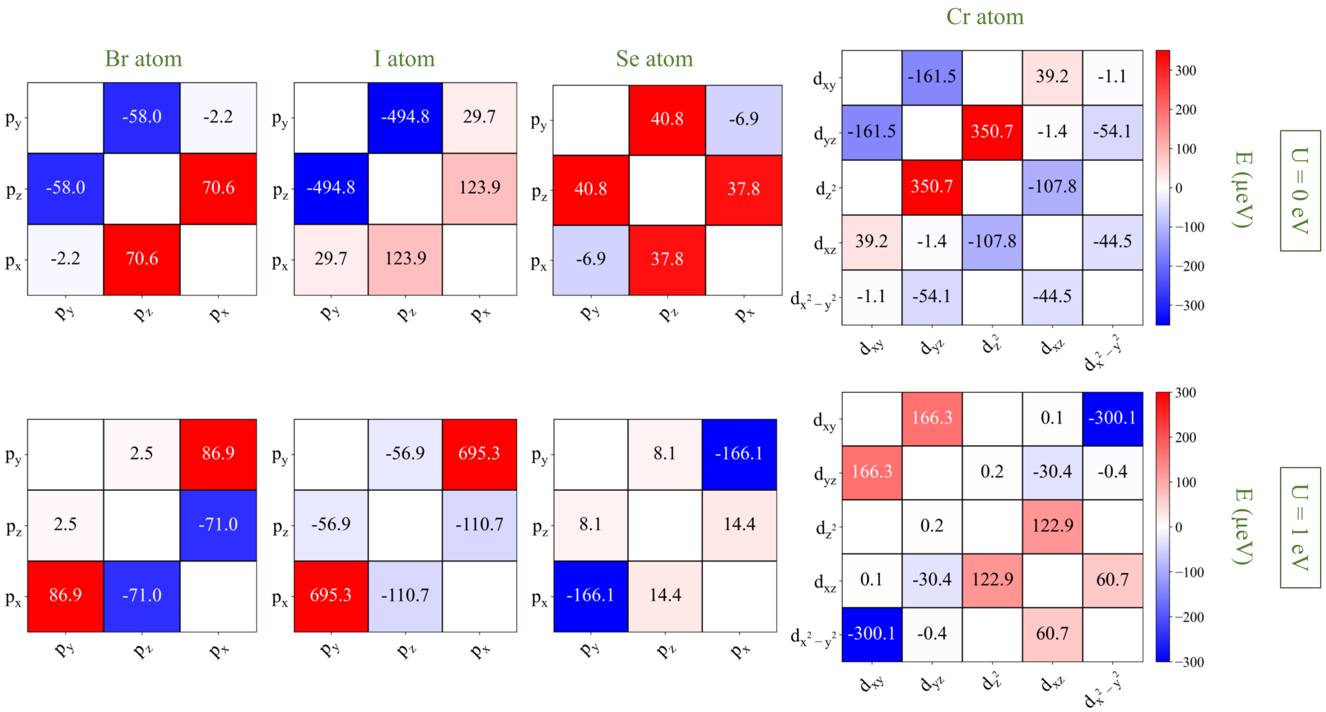

U = 0 eV

Br atom	p_y	p_z	p_x
p_y		-58.0	-2.2
p_z	-58.0		70.6
p_x	-2.2	70.6	

I atom	p_y	p_z	p_x
p_y		-494.8	29.7
p_z	-494.8		123.9
p_x	29.7	123.9	

Se atom	p_y	p_z	p_x
p_y		40.8	-6.9
p_z	40.8		37.8
p_x	-6.9	37.8	

Cr atom	d_{xy}	d_{yz}	d_{z^2}	d_{xz}	$d_{x^2-y^2}$
d_{xy}		-161.5		39.2	-1.1
d_{yz}	-161.5		350.7	-1.4	-54.1
d_{z^2}		350.7		-107.8	
d_{xz}	39.2	-1.4	-107.8		-44.5
$d_{x^2-y^2}$	-1.1	-54.1		-44.5	

U = 1 eV

Br atom	p_y	p_z	p_x
p_y		2.5	86.9
p_z	2.5		-71.0
p_x	86.9	-71.0	

I atom	p_y	p_z	p_x
p_y		-56.9	695.3
p_z	-56.9		-110.7
p_x	695.3	-110.7	

Se atom	p_y	p_z	p_x
p_y		8.1	-166.1
p_z	8.1		14.4
p_x	-166.1	14.4	

Cr atom	d_{xy}	d_{yz}	d_{z^2}	d_{xz}	$d_{x^2-y^2}$
d_{xy}		166.3		0.1	-300.1
d_{yz}	166.3		0.2	-30.4	-0.4
d_{z^2}		0.2		122.9	
d_{xz}	0.1	-30.4	122.9		60.7
$d_{x^2-y^2}$	-300.1	-0.4		60.7	

FIG. S14. Orbital-projected contributions of spin–orbit coupling (SOC) from Cr-3d, Br-2p, I-2p, and Se-4p states to the magnetocrystalline anisotropy energy (MAE) for Cr_2BrISe_2 at U = 0 and 1 eV, where a change in the magnetic easy axis is observed.